Molecular Catalysis 518 (2022) 112085

Contents lists available at ScienceDirect

Molecular Catalysis

journal homepage: www.journals.elsevier.com/molecular-catalysis

In situ DRIFTS and CO-TPD studies of CeO_2 and SiO_2 supported CuO_x catalysts for CO oxidation

Md Robayet Ahasan, Yifan Wang, Ruigang Wang *

Department of Metallurgical and Materials Engineering, The University of Alabama, Tuscaloosa, AL 35487, United States

ARTICLE INFO

Keywords:
CuO_x/CeO_2
CO-TPD
DRIFTS
H_2-TPR
CO oxidation

ABSTRACT

Gas adsorption-desorption processes on oxide supported metal catalysts are critical steps for understanding catalytic CO oxidation mechanism. This report investigates the support structure (shape and exposed crystal planes)-catalytic activity relationship of irreducible SiO_2 and reducible CeO_2 nanorods (NR) and nanocubes (NC) supported CuO_x via various structural and surface characterization methods, including XRD, Raman spectroscopy, BET surface area, H_2-TPR, CO-TPD, *in situ* DRIFTS, XPS, and HRTEM. Evidence is presented that both isolated Cu^+/Cu^{2+} redox pair and lattice oxygen of oxide supports from different crystal planes (111, 011, and 001) of CeO_2 play important role towards CO oxidation by supporting Langmuir–Hinshelwood mechanism. The Cu^+/Cu^{2+} and Ce^{3+}/Ce^{4+} species at CuO_x-CeO_2 interfaces can facilitate the charge and mass transfer between CuO_x nanoclusters and CeO_2 by electronic interaction which was highly promoted by reducible CeO_2 NR support. In addition, CeO_2 NR contains significantly higher amount of surface defects including oxygen vacancy, steps, voids, and lattice distortion on various crystal facets, which promote surface oxygen release of CeO_2 and CO adsorption and oxidation on catalytically active sites at lower temperature. According to the CO oxidation results, the oxidized CuO/CeO_2 NR sample showed 62.8% CO conversion at 100°C and up to 98.9% conversion at 397 °C.

1. Introduction

Supported transition metal (TM) oxides are now considered as highly preferential low-cost catalysts for a wide range of oxidation applications such as in CO oxidation, water gas shift reaction and automotive exhaust three-way catalytic conversion [1, 2]. Recently, oxide supports with superior oxygen storage capacity (OSC) or surface oxygen mobility have attracted increasing attention for further promoting the redox-related catalytic activity of TM oxide based catalysts [3]. The OSC or oxygen mobility properties can be defined by oxygen adsorption/desorption rate, capacity, and surface oxygen exchange rate between gaseous oxygen and catalyst/support surface. For example, Co_3O_4 based catalysts (Co_3O_4 nanorods, Au_1/Co_3O_4, and In_2O_3/Co_3O_4) have been widely investigated for low temperature CO oxidation due to the atomic level surface oxygen activation and exchange capability [4–6]. Among various oxide supports, such as Al_2O_3, SiO_2, CeO_2, ZrO_2, HfO_2, and ThO_2 or their mixed oxides (i.e., CeO_2−ZrO_2) [7], shape-controlled and surface engineered CeO_2 has been widely utilized in several catalytic reactions and platforms due to its fast reversible change of Ce oxidation state between +4 and +3, high oxygen storage and release capacity, easy surface oxygen mobility, facile oxygen vacancy formation on different low-index surfaces of CeO_2 ({100}, {110}, and {111}), and narrow Ce-4f band [8].

Based on the concepts of surface engineering and elemental doping, a number of published studies describe that CeO_2 nanocrystals were enriched with surface oxygen vacancy and other defects, which are attributed to facilitating the reduction of adjacent Ce^{4+} to Ce^{3+}. Generally speaking, Ce^{3+} concentration is proportional to oxygen vacancy concentration as well as related to the effectiveness of oxygen exchange between catalyst and support [9]. Moreover, it was claimed that the occupied 4f-orbital electrons of Ce^{3+} ions could promote electronic interaction between reducible CeO_2 and metal nanoparticles [10]. As a result of this unique OSC property, reducible CeO_2-based oxides have been utilized in versatile technological applications, such as in oxygen sensors, solid oxide fuel cells (SOFC), water gas shift reaction, and most importantly vehicle catalytic converters [11].

On the other side, irreducible SiO_2 has been another frequently used oxide catalyst support, which possesses high surface area and good

* Corresponding author.
E-mail address: rwang@eng.ua.edu (R. Wang).

https://doi.org/10.1016/j.mcat.2021.112085
Received 29 October 2021; Received in revised form 16 December 2021; Accepted 17 December 2021

thermal stability that can enhance the dispersion of metal clusters. However, due to the high oxygen vacancy formation energy and low isoelectric point (IEP) of SiO_2 (IEP ~x223C 2), it is in general considered as an inert catalyst support in nature and forms weak or no interaction with metal catalyst clusters [12]. Besides, previous research has established that porous structure of SiO_2 support favors to form filamentous cokes with low activation and their easy displacement towards the catalyst particle exterior [13].

Cu based catalysts have been extensively used in water–gas shift reaction [14], methane reformation [15] and NO_x elimination [16]. It is now well established that, from kinetics and mechanism aspects, Cu catalysts (Cu–Cu_2O–CuO system) have demonstrated noticeable performance on low temperature CO oxidation [17]. Jia et al. [18] compared the CO oxidation activity between 5 wt% CuO@CeO_2 (CuO crystallite size of 4.1 nm) and inverse 5 wt% CeO_2@CuO (CeO_2 crystallite size of 4.0 nm) catalysts and concluded that the reaction may occur at the interface of CuO-CeO_2. Similar results were also reported by Luo et al. [19], where they demonstrated that nano-sized CuO/CeO_2 catalysts with higher surface area (> 90 m^2/g and finely dispersed CuO crystallites) had better CO oxidation activity (183.3 $mmol_{CO}\ g_{Cu}{}^{-1}h^{-1}$) than bulk CuO crystallites (100.4 $mmol_{CO}\ g_{Cu}{}^{-1}h^{-1}$). In addition, high temperature thermal treatments (oxidation or reduction) could facilitate the diffusion or migration of the Cu^+/Cu^{2+} species into CeO_2 lattice (i.e., formation of Cu-O-Ce bond) and optimal thermal treatments could also "activate" finely dispersed CuO crystallites anchoring them tightly on CeO_2 supports [17–20].

Despite the importance of catalyst-support interaction, a fundamental understanding of CO adsorption-desorption processes on different oxide supported metal catalysts with strong or weak interplay is still lacking. Such insights will provide a clarification of active sites nature and possible reaction mechanism for CO oxidation.

In this work, we present a detailed study of CO temperature programmed desorption (CO-TPD) and *in situ* Diffuse Reflectance Infrared Fourier Transform Spectroscopy (DRIFTS) characterization to obtain qualitative and quantitative surface information of gas-solid interaction on irreducible SiO_2 and reducible CeO_2 supported 10 wt% of CuO_x catalyst.

2. Experimental section

2.1. Catalyst preparation

2.1.1. Preparation of catalyst supports

In our experiments, three different catalyst supports were synthesized including CeO_2 nanorods (NR), CeO_2 nanocubes (NC) and amorphous SiO_2. Both CeO_2 NR and CeO_2 NC were prepared by a hydrothermal method according to our previous research methodology [21]. To obtain CeO_2 NR, first of all, 88 mL of 0.1 M $Ce(NO_3)_3{\bullet}6H_2O$ (Acros Organics, 99.5%) was mixed properly with 8 mL of 6.0 M NaOH (VWR, 99%) solution in a 200 mL Teflon liner and stirred for ~x223C15 s. The Teflon liner was then put into a stainless-steel autoclave and sealed tightly. The autoclave was heated and kept at 90°C for 48 hours. The precipitate materials were washed thoroughly with distilled water to remove any residual ions (Na^+, NO_3^-), then washed with ethanol to avoid hard agglomeration of the nanoparticles and dried in air at 60°C for 12 h. The dried sample was collected and ground gently with mortar and pestle. Similar procedure was also followed for the preparation of CeO_2 NC, however the autoclave was kept at 150°C for 48 h. SiO_2 support was prepared by hydrolysis method. Here, tetraethyl orthosilicate (1.5 mL; TEOS, Acros Organics, 98%) was first dissolved in a mixture of 50 mL of ethanol and 1 mL of deionized water in a 100 mL beaker and heated to 50°C. Then, 1.5 mL of ammonia solution ($NH_3{\bullet}H_2O$, BDH, 28–30 vol%) was added dropwise to the above solution under vigorous magnetic stirring and lasted for another 24 h at 50°C to get complete hydrolysis. SiO_2 powder was finally obtained by placing the white suspension solution in a drying oven at 60°C overnight.

2.1.2. Preparation of supported catalysts

Based on our previous studies [17, 19], 10 wt% CuO was loaded onto the CeO_2 and SiO_2 supports using wet impregnation method. Typically, both CeO_2 and SiO_2 supports, 0.9 g each, were suspended into 100 mL deionized water separately in three 200 mL beakers. Then, 0.366 g of $Cu(NO_3)_2{\cdot}2.5H_2O$ (Alfa Aesar) (10 wt%) was dissolved in each solution. During the stirring process for mixing, 0.5 M aqueous solution of ammonium hydroxide ($NH_3{\cdot}H_2O$, BDH, 28-30 vol%) was added dropwise into the mixture until the pH achieved ~x223C9. After that, the solution was aged under stirring (400 rpm) at 80°C for 4 h and placed in a drying oven to evaporate water. The collected sample was ground with mortar and pestle and calcined at 350°C for 5 h. Half of the resultant samples was further reduced in a tube furnace under 5 vol% H_2/95 vol% He atmosphere at 300°C for 5 h. In the following, "o" in the sample's name refers to the oxidized sample (i.e., 10 wt% CuO/CeO_2 NR-o) and "r" in the sample's name refers to the reduced sample (i.e., 10 wt% CuO/CeO_2 NR-r). No other pretreatment was applied before the characterizations of CO-TPD, XPS, Raman spectroscopy, and DRIFTS.

2.2. Catalyst characterization

Powder X-ray diffraction (XRD) characterization was performed on a Phillips X'Pert MPD diffractometer with a copper Kα radiation source (λ=0.154 nm) at 40 kV and 40 mA. The samples were scanned in the 2θ range between 10 ° and 90 ° with a scan rate of 0.5° min^{-1}. The lattice parameters and average crystallite size of each catalyst sample were estimated by JADE software according to the recorded XRD patterns.

The BET surface area was measured with nitrogen physisorption at ~x223C77 K. H_2-temperature programmed reduction (H_2-TPR) characterization was performed with a Micromeritics AutoChem II 2920 chemisorption analyzer. The powder samples (85-95 mg) were put into a quartz U-tube sandwiched by two pieces of quartz wools followed by heating from 30°C to 900°C at a heating rate of 10°C/min. The samples were reduced under 10 vol% H_2- 90 vol% Ar gas mixture with a flow rate of 50 mL/min. The amount of H_2 uptake during the reduction was measured by a thermal conductivity detector (TCD), which was calibrated by a quantitative reduction of CuO to metallic copper.

Carbon monoxide temperature-programmed desorption (CO-TPD) was performed using the same instrument (Micromeritics AutoChem II 2920) as H_2-TPR to investigate the interaction of CO with the catalyst/support surface. Powder sample was put into a quartz U-tube micro reactor and heated in He stream (flowrate: 50 mL/min) from room temperature to 400°C to remove residual moisture. After the sample was cooled to room temperature, 10 vol% CO - 90 vol% He mixture gas was flowed at 50 mL/min through the sample for 60 min. The sample was then ramped up to 800°C at a linear heating rate of 10°C/min again under helium gas and the desorption behavior of CO was monitored by a thermal conductivity detector at elevated temperatures.

Transmission electron microscopy (TEM) images were obtained by using a FEG-TEM instrument (FEI Tecnai F20) with an acceleration voltage of 200 kV and energy dispersive X-ray spectroscopy data (EDAX system) was collected on JEOL 7000 FE SEM. The TEM samples were prepared by ultrasonic dispersion of the powders in ethanol and one or two drops of the suspension solution were deposited on ultrathin carbon film supported by a 400-mesh copper grid (Ted Pella Inc.) and then dried for 2 h before analysis.

X-ray photoelectron spectroscopy (XPS) data was recorded by Kratos Axis Ultra DLD spectrometer using monochromatic Al Kα (hv = 1486.6 eV) source under ultra-high vacuum (10^{-10} Torr), and the binding energies (BE) were calibrated internally by the carbon deposit C 1s at 284.8 eV. The fitting and deconvolution of the spectra were conducted using the CASA XPS software.

Raman spectra for the catalysts were collected using Horiba LabRAM HR 800 Raman spectrometer (equipped with a 100 long working distance objective, NA= 0.60) in the spectral window from 100 to 1200 cm^{-1}. A diode-pumped solid-state (DPSS) laser system (Laser Quantum

MPC6000) tuned at λ = 532 nm was used for excitation. Prior to each analysis, the spectrometer was calibrated using a single crystal Si wafer. *In situ* diffuse reflectance IR Fourier transform spectroscopy (DRIFTS) measurements of CO chemisorption over the samples were recorded on a Nicolet 6700 Fourier-transform infrared spectroscopy (FTIR) spectrometer equipped with a Harrick Praying Mantis DRIFTS accessory, with a resolution of 4 cm^{-1}.

2.3. Catalytic activity measurements

Catalytic activity measurements for CO oxidation were carried out in a downward fixed bed glass tubular reactor using ~x223C50 mg catalyst sample sandwiched by two pieces of quartz wools. The catalysts were directly exposed to gas mixture of 1 vol% CO, 20 vol% O_2, and 79 vol% He at a flow rate of 38 mL/min with a corresponding weight hour space velocity (WHSV) value of 76,000 mL h^{-1} g_{cat}^{-1}, without any pretreatment. The reaction temperature was programmed from room temperature to 400°C while CO and CO_2 concentrations in the reactor effluent were analyzed by an online gas chromatograph (SRI multiple gas analyzer GC, chassis). The CO conversion was evaluated by the following equation:

$$\text{CO conversion } (\%) = \frac{[CO]_{inlet} - [CO]_{outlet}}{[CO]_{inlet}} * 100\%$$

Here, $[CO]_{inlet}$ is input concentration of CO gas and $[CO]_{outlet}$ is output concentration of CO gas.

3. Results and discussion

3.1. XRD analysis

Fig. 1(a) shows the XRD profiles for three oxide supports: irreducible SiO_2 and reducible CeO_2 with two different morphologies (CeO_2 nanorods: CeO_2 NR and CeO_2 nanocubes: CeO_2 NC). For SiO_2, the broad diffuse peak centered at 22.1° confirms the presence of amorphous silica structure [22]. The CeO_2 NR and CeO_2 NC samples show a series of diffraction peaks at 28.6°, 33.1°, 47.6°, 56.3° which match with (111), (200), (220) and (311) crystal planes respectively of face-centered cubic fluorite-type CeO_2 structure from the JCPDS database (#34-0394). It is also noticeable that the diffraction peaks of CeO_2 NC are sharper than those of CeO_2 NR, which indicates that CeO_2 NC has better crystallinity and larger crystallite size than CeO_2 NR [23].

The XRD profiles of SiO_2, CeO_2 NR and NC supported CuO_x catalysts, for both oxidized and reduced samples, are shown in Fig. 1(b-c). Similarly, fluorite-type structure was also observed for CeO_2 NR and CeO_2 NC in the supported CuO_x catalysts, indicating that no apparent structural change of CeO_2 supports occurred during the catalyst loading and thermal treatments under oxidation and reduction atmosphere. For the CeO_2 supported catalysts, two broad diffraction peaks corresponding to (002) and (111) planes of monoclinic CuO with very low intensity were observed, as shown Fig. 1(b) and (d). Using the Scherrer equation, the estimated crystallite size of CeO_2 NR is 6.4 nm, which is much smaller than that of CeO_2 NC (17.1 nm). The smaller crystallite size of CeO_2 NR

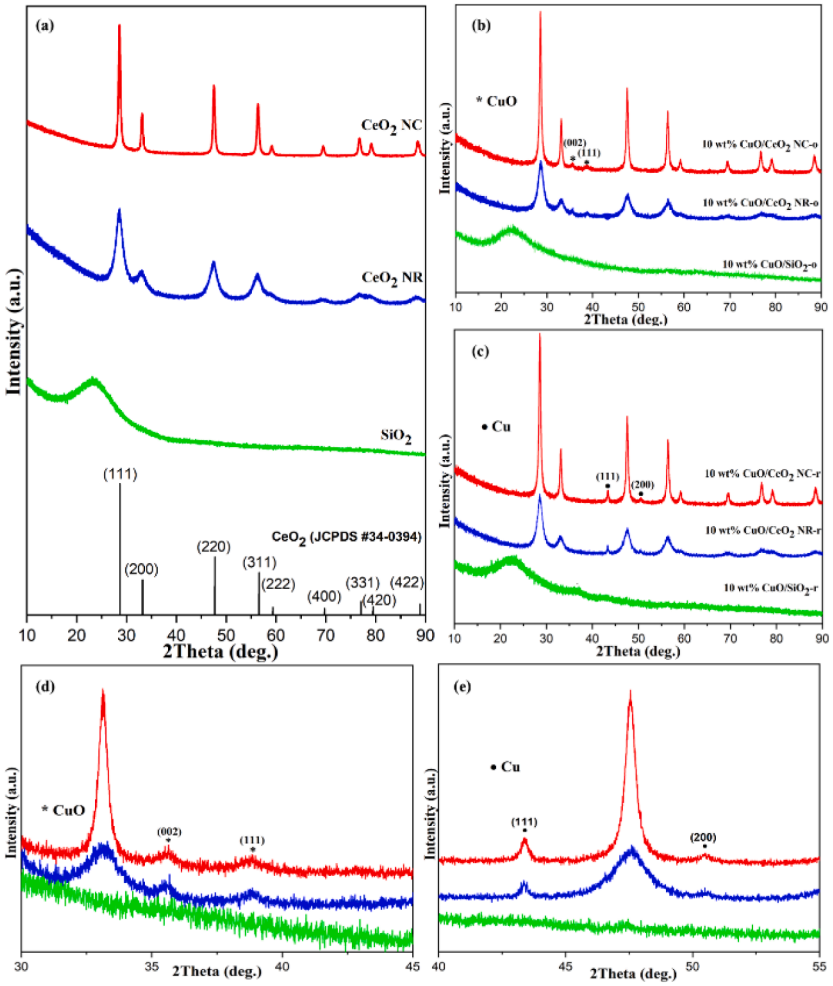

Fig. 1. XRD patterns of (a) CeO_2 NR, CeO_2 NC and SiO_2 supports, (b) supported CuO_x catalysts after oxidation treatment, (c) supported CuO_x catalysts after reduction treatment and (d-e) enlarged XRD patterns from (b-c).

agrees well with its higher BET surface area (112.9 m^2/g) compared to CeO_2 NC. After the deposition of CuO_x, the estimated crystallite sizes of CeO_2 in 10 wt% CuO/CeO_2 NR-o and 10 wt% CuO/CeO_2 NC-o are 6.6 nm and 17.2 nm respectively. After the reduction treatment, the estimated crystalline sizes of CeO_2 in 10 wt% CuO/CeO_2 NR and 10 wt% CuO/CeO_2 NC are 6.7 nm and 17.3 nm respectively. The crystalline sizes of CuO and Cu in 10 wt% CuO/CeO_2 NR-o were also calculated using Scherrer equation, which were 2.5 nm and 3.3 nm respectively. The observed low peak intensity of CuO is partially due to the strong interaction between CuO_x clusters with CeO_2 supports [24]. However, no apparent diffraction peaks of CuO_x are present for both oxidized and reduced CuO_x/SiO_2. Several possible explanations for this absence of CuO_x diffraction peaks in the prepared CuO_x/SiO_2 catalysts might be: 1) the amorphous nature of copper-related species; 2) tiny CuO_x crystallites buried in amorphous silica matrix; 3) the formation of Cu-O-Si amorphous structure in porous silica [25]. A similar result was also reported previously by Lu et al. [26], where they showed no evidence of CuO diffraction peaks for CuO/SiO_2 at low CuO loadings (<5 wt%) and concluded that crystalline CuO can be observed at higher CuO loading greater than 10 wt%. To further confirm the presence of copper species, EDX line spectrum and elemental mapping were carried out. Clearly, from the EDX spectrum and elemental mappings of Fig. 2 from several randomly selected areas of CuO_x/SiO_2, it displays a uniform distribution of copper.

After the reduction treatment at 300°C under 5 vol% H_2/95 vol% He, the XRD patterns for three supported CuO_x catalysts are given in Fig. 1 (c). After the reduction treatment, metallic Cu phase is identified in both CuO_x/CeO_2 catalysts. However, the intensity of Cu diffraction peaks is much weaker for the CeO_2 NR supported CuO_x sample suggesting a stronger CuO_x-CeO_2 interaction for the CeO_2 NR sample. This can be observed clearly in the expanded and zoomed region shown in Fig. 1(e). Fig. 1(d, e) were replotted from Fig. 1(b, c) for the oxidized and reduced catalysts. Two CuO diffraction peaks at 35.5° and 38.75° corresponding to (002) and (111) planes for the oxidized sample are clearly observed in Fig. 1(d), while for the reduced sample two Cu the diffraction peaks at 43.0° and 50.5° corresponding to (111) and (200) planes of Cu ensure a complete reduction from CuO to Cu.

Since the CuO loading was 10 wt% for both CeO_2 NR and NC samples, the XRD results suggest a better dispersion and smaller crystalline size of CuO_x on CeO_2 NR support. In addition, it is also possible that during the reduction treatment, some CuO_x clusters diffuse into the lattice of CeO_2 NR (with rich surface defects and oxygen vacancy) and form Cu-O-Ce solid solution. All of these can lead to the reduced XRD peak intensity of CuO_x clusters on CeO_2 NR support.

3.2. H_2-TPR and BET surface area measurement

The H_2-TPR profiles of SiO_2, CeO_2 NR and CeO_2 NC supports are shown in Fig. 3(a). For two CeO_2 supports, the low temperature region peaks (200~x223C600 °C) are attributed to the surface reduction from Ce^{4+} to Ce^{3+} (for CeO_2 NR: 350 °C and 486 °C; for CeO_2 NC: 408 °C and 535 °C). The high temperature region peak (>600 °C) that belongs to the bulk reduction of Ce^{4+} is centered at 745 °C and 779 °C for CeO_2 NR and CeO_2 NC, respectively. No apparent reduction or hydrogen consumption peak is observed for SiO_2 as expected as SiO_2 has high oxygen vacancy formation energy (~x223C9.6 eV) and is an irreducible oxide [27]. Based on the results of the surface reduction temperature and hydrogen consumption, the reducibility order of these three catalyst supports is as follows: CeO_2 NR > CeO_2 NC >> SiO_2. It has been reported that the possible origins of the superior low temperature reducibility of CeO_2 NR are attributed to its highly active (100) and (110) surface planes as well as contributory amount of (111) surface defects [28].

Table 2 summarizes the quantitative hydrogen consumption data calculated from the H_2-TPR profiles of each sample. For the 10 wt% CuO/SiO_2-o catalyst in Fig. 3(b), the peak at 197°C is assigned for the reduction of CuO species. An very weak peak at 514°C was observed which could be due to the reduction of larger size CuO clusters or CeO_2 support. For the 10 wt% CuO/CeO_2 NR-o and 10 wt% CuO/CeO_2 NC-o samples, Fig. 3(b) illustrates two low temperature peaks (<200°C) that belong to two-step (sometimes three-step) reduction reported in literature. In the two-step reduction profile, the low-temperature peak is assigned to the smaller, well-dispersed and strongly interacting crystalline CuO_x with CeO_2 support while the higher temperature peak is attributed to "bulk-like" larger CuO_x particles that interact weakly with CeO_2 support [24]. Thus, in this study, for 10 wt% CuO/CeO_2 NR-o, the low temperature reduction peak at 145°C (called α peak) is due to the strong interaction of small and well-dispersed CuO_x species with CeO_2 NR, while the reduction peak at 171°C (known as β peak) belongs to highly dispersed CuO_x weakly interacting with CeO_2 NR. This α peak often indicates the formation of Cu-O-Ce solid solution. Similar assignments are applied to the 10 wt% CuO/CeO_2 NC-o sample, where two types of reduction peaks are at 155°C and 193°C. It is very clear that the higher H_2 consumption (2727.25 μmol/g) and lower reduction temperature (171°C) of the 10 wt% CuO/CeO_2 NR-o sample indicate a superior low temperature reducibility compared to the 10 wt% CuO/CeO_2 NC-o sample. This definitely demonstrates the support morphology

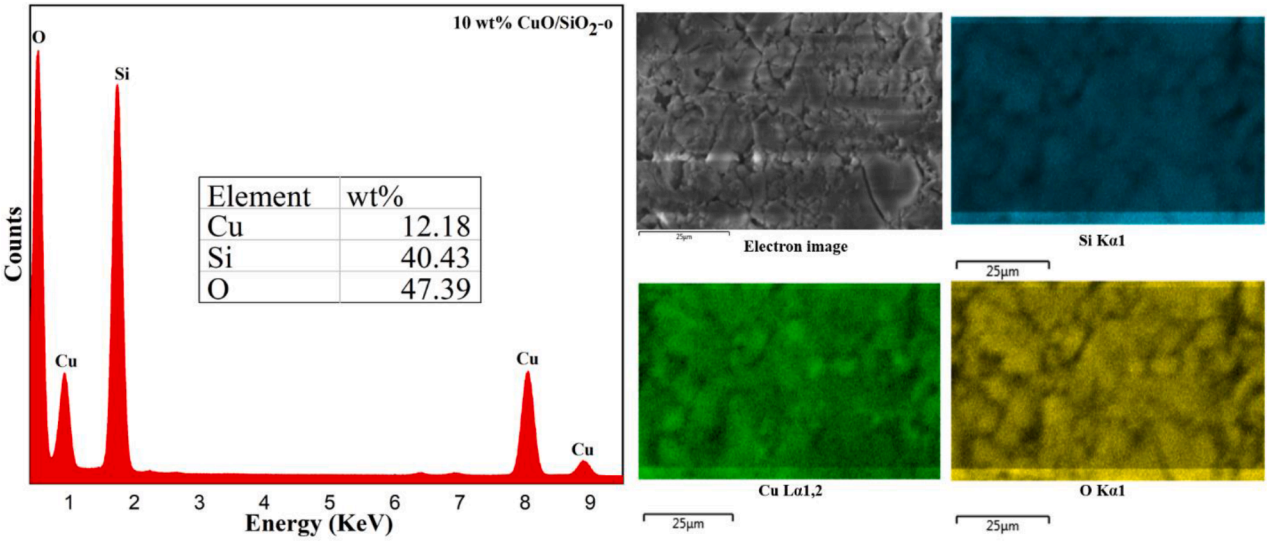

Fig. 2. EDS line spectrum and elemental mapping of 10 wt% CuO/SiO_2-o catalyst.

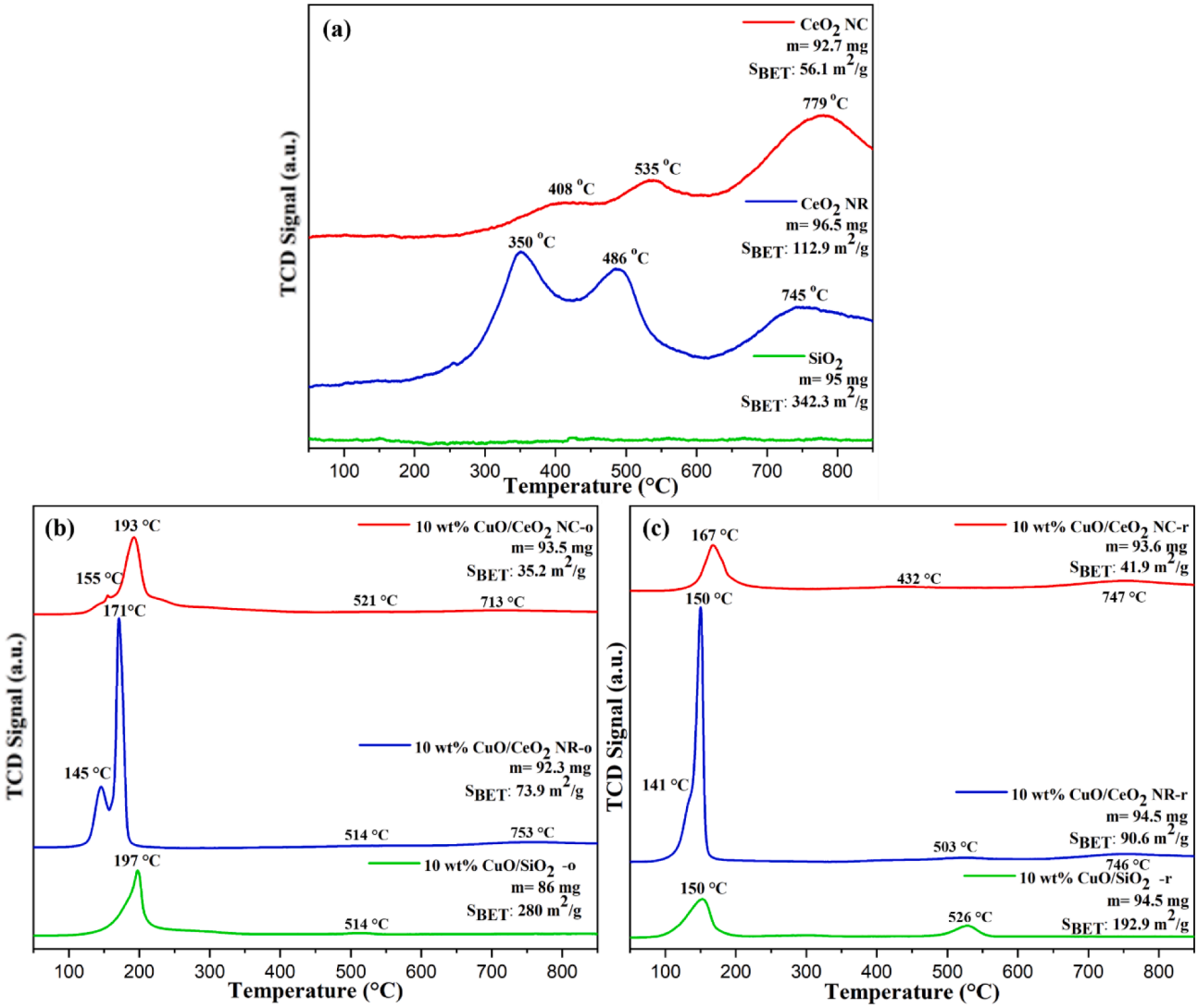

Fig. 3. H_2-TPR profiles of (a) SiO_2, CeO_2 NR and CeO_2 NC supports, (b) supported CuO_x catalysts after oxidation treatment and (c) supported CuO_x catalysts after reduction treatment.

effect (CeO_2 NR vs. CeO_2 NC) on the activity of CuO_x catalyst. It should be pointed out that Fig. 3(a) has different scale factors compared to Fig. 3(b, c), so some high temperature hydrogen consumption peaks (>800°C) are too weak to be visible in the present scale due to the dominant surface H_2 consumption (<250°C), but the quantitative H_2 uptakes are included in Table 1.

After the reduction treatment, all three samples show some small changes in terms of hydrogen consumption and reduction temperature. For example, all three samples showed at least 36% reduced hydrogen consumption (Table 1). This is obviouslly attributed to the reduction of CuO to Cu. In fact, the α and β type peaks also merge together after the reduction treatment indicating the ionic diffusion during the reduction treatment [29].

3.3. CO-TPD characterization

Fig. 4 shows the CO-TPD results to quantify the nature of CO interaction with three catalysts. In general, the CO-TPD profile is quantified

Table 1
H_2 consumption, and reduction temperature of the prepared samples from the H_2-TPR profiles.

Samples	H_2 consumption (μmol/g)			Peak temperature (° C)	
	Surface reduction, S_r	Bulk reduction, B_r	Total	Initial reduction temperature (° C)	S_r	B_r
SiO_2	0	0	0	0	0	0
CeO_2 NR	675.6	364.1	1039.7	54	350	745
CeO_2 NC	354.3	545.9	900.2	45	408	779
10 wt% CuO/SiO_2-o	1283.4	383.6	1667.0	85	197	514
10 wt% CuO/CeO_2 NR-o	1954.2	773.1	2727.2	89	171	761
10 wt% CuO/CeO_2 NC-o	1845.3	581.2	2426.6	82	193	708
10 wt% CuO/SiO_2-r	528.7	281.9	810.6	60	150	526
10 wt% CuO/CeO_2 NR-r	1123.2	599.7	1722.9	76	150	756
10 wt% CuO/CeO_2 NC-r	529.8	810.7	1340.5	81	167	750

Table 2
Vibration frequencies and bond assignments of adsorbed or formed species over the 10 wt%CuO/CeO_2 NR catalysts.

Species	Bond types	Frequency (cm^{-1}) 10 wt% CuO/CeO_2 NR	References
Absorbed CO	Cu-CO	2113	[35–38]
Surface oxo species	Formate	1351	
	Bridged carbonate	1392	
	Bridged carboxylate	1544	
		1062, 1216, 1297, 1574,	
	Bi or tri carbonates	1612	

by desorbing CO_2 gas from the catalyst surface at elevated temperature [29].

It is evident from Fig. 4 that a considerable amount of CO desorbed as CO_2 from each catalyst surface while 10 wt% CuO/CeO_2 NR-o showed the highest CO_2 desorption at the lowest temperature, indicating easy accessible surface oxygen which is possibly due to the strong interaction of CuO with CeO_2 NR. Below 400 °C, the 10 wt% CuO/CeO_2 NR-o sample presents two CO_2 desorption peak at 89 °C and 270 °C while the other two samples have only one desorption peak at 89 °C for 10 wt % CuO/SiO_2-o and 90 °C for 10 wt% CuO/CeO_2 NC-o. A similar result (with a little higher desorption temperature) was also reported by Liu et al. [30]. From the previous simulation and experimental studies of CeO_2 based catalysts [31–34], both weak and strong adsorptions of CO co-exist on the {1 1 0} plane and strong adsorption belongs to the {1 0 0} plane. This strong adsorption is due to the developed bidenate carbonate species by CO on CeO_2 surfaces [31]. Accordingly, in this study, the peak at 89°C is attributed to the mixed weak and strong adsorption of CO with exposed (110) plane while the peak at 270°C is assigned to the strong CO adsorption on (100) plane of CeO_2 NR surface. Both 10 wt% CuO/SiO_2-o and 10 wt% CuO/CeO_2 NC-o showed one single desorption peak (<400°C), however, the intensity is relatively low. Furthermore, the stronger desorption peak for 10 wt% CuO/CeO_2 NR-o is consistent with the H_2-TPR result (Fig. 3) which indicates 10 wt% CuO/CeO_2 NR-o contains larger amounts of active surface oxygen [35–36]. After the reduction treatment, single desorption peak was observed for each sample from 70°C to 200°C. This observation confirms that the surface accessible oxygen species in oxide supported CuO_x catalysts affect the CO adsorption and desorption processes and a careful selection of catalyst support is important for better low temperature catalyst performance.

3.4. Raman spectroscopy analysis

Besides XRD analysis, Raman spectroscopy is also a favorable structural characterization technique owing to its sensitivity to crystalline symmetry and oxygen lattice vibrations [33]. In our experiment, the Raman spectra were collected by using a laser at 532 nm as the excitation source.

As shown in Fig. 5, the strongest peaks centered at ~x223C443 and ~x223C454 cm^{-1}, for the oxide and reduced samples respectively, correspond to the triply degenerate F_{2g} vibrational mode of fluorite CeO_2 where symmetrical stretching vibration of the O ions happens around the Ce ions [34]. In addition, Raman spectra for both samples show a minor peak (~x223C268 cm^{-1}) as well as a shoulder peak around 556 cm^{-1}. The shoulder peak at 556 cm^{-1} and weak broad peak 268 cm^{-1} can be attributed to the formation of oxygen vacancy and/or presence of structural defects in the CeO_2 lattice [31, 32]. The formation of oxygen vacancy is partially due to the incorporation of Cu^{2+}/Cu^{+} in CeO_2 lattice [37–41]. According to literature, typical peaks at 271, 326, 506, and 625 cm^{-1} represent the A_g, B_{1g}, B_{2u}, and B_{2g} mode for CuO. However, in our case, no obvious peaks for CuO were found from the Raman spectra of the CuO/CeO_2 NR-o catalysts, which indicates a possibility of the formation of Cu-O-Ce bonding or solid solution [42]. In addition, from Fig. 5, the noticeable difference from the Raman spectra of the two samples are position and the width or FWHM (47.65 cm^{-1} for 10 wt% CuO/CeO_2 NR-o and 37.35 cm^{-1} for 10 wt% CuO/CeO_2 NR-r). A red shift of the reduced 10 wt% CuO/CeO_2 NR sample is observed which represents the improved crystallinity and/or large crystalline size of the supported CuO_x catalyst.

3.5. XPS analysis

The XPS spectra for the oxidized and reduced 10 wt% CuO/CeO_2 NR samples are exhibited in Fig. 6 to identify the surface composition, oxidation state (Ce^{3+}/Ce^{4+} and Cu^{2+}/Cu^{+}), and different oxygen types (lattice oxygen and oxygen vacancy). The XPS spectra of Ce 3d, O 1s and Cu 2p are shown in Fig. 6(a, b), Fig. 6(c, d) and Fig. 6(e, f) respectively. Standard calibration for the binding energy was done by C 1s peak at 284.8 eV.

From the Ce 3d XPS spectra in Fig. 6(a, b), both the oxidized and reduced samples compose of two u and v multiplets that belong to spin orbit split of $3d_{3/2}$ and $3d_{5/2}$ respectively. Six peaks corresponding to $3d_{3/2}$ and $3d_{5/2}$ doublets are labeled as U′, U″, U‴, V′, V″ and V‴. All these peaks can be assigned for the Ce^{4+} state while the low intensity shoulder peaks labeled as U and V next to U′ and V′ are assigned for the

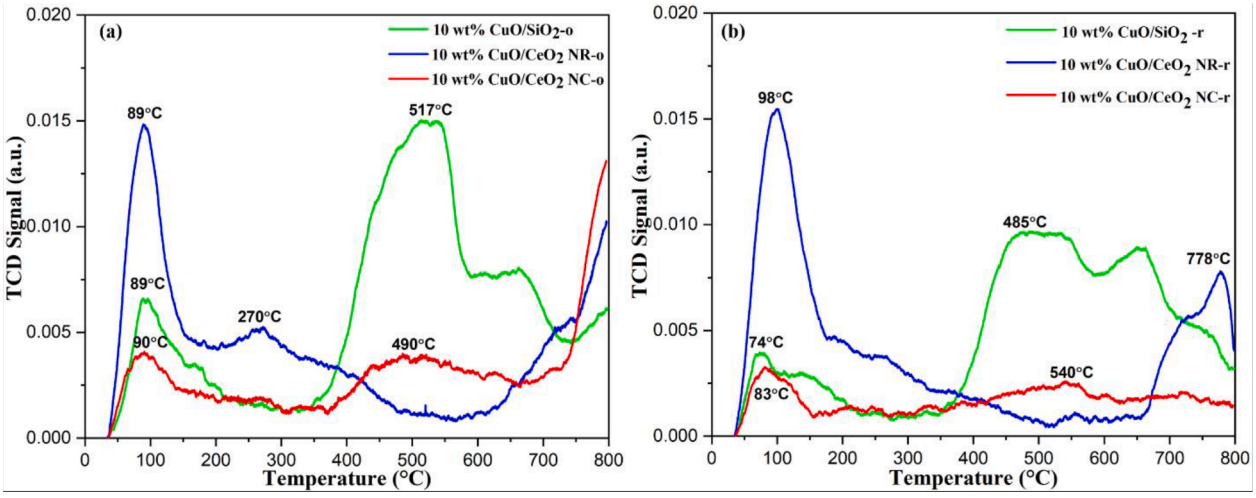

Fig. 4. CO-TPD profiles of (a) SiO_2, CeO_2 NR & CeO_2 NC supported CuO catalysts after oxidation treatment, (b) SiO_2, CeO_2 NR & CeO_2 NC supported CuO catalysts after reduction treatment.

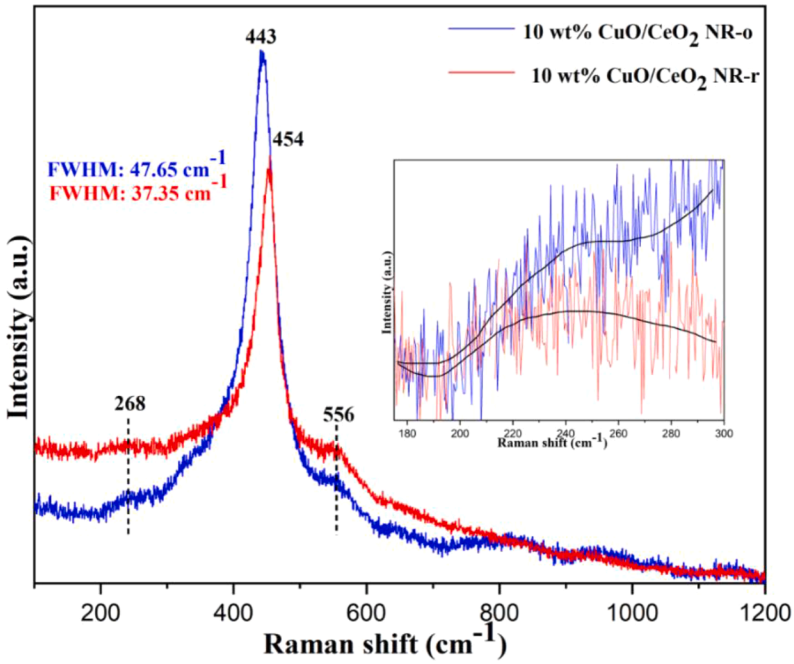

Fig. 5. Raman spectroscopy profiles of the 10 wt% CuO/CeO_2 NR-o & 10 wt% CuO/CeO_2 NR-r samples.

Ce^{3+} state [25, 26]. It is known that U‴ and V‴ peaks are called satellite peaks that represent the presence of Ce^{4+} ion which is attributed to energy gain (shake-down) process and known as "shake-down" states [40]. For both of the samples, there is a noticeable presence of Ce^{3+} ion from the XPS spectra of Ce 3d (~x223C20% Ce^{3+}). This observation agrees with the CO oxidation results below as the Ce^{3+} ion concentration plays a key role in CO conversion as previously reported [41]. Fig. 6(c, d) show the XPS spectra for O 1s. The main peaks at 528.3 eV corresponds to the lattice oxygen and the left shoulder peak with low intensity and higher binding energy (530.3 eV) represents the surface oxygen vacancy of the supported catalysts. Based on the integrated peak area of O 1s, it was calculated that the oxygen vacancy concentration of 10 wt% CuO/CeO_2 NR-o is higher than that of 10 wt% CuO/CeO_2 NR-r, indicating more surface oxygen in the oxidized sample can contribute to the CO oxidation reaction. Fig. 6(e, f) reveal the Cu 2p XPS spectra of the oxidized and reduced samples while two peaks at 933.1 and 953.1 eV represent the Cu $2P_{3/2}$ and Cu $2P_{1/2}$ respectively. The distance between these two peaks is 20 eV which confirms the presence of CuO in the oxidized sample. It can be seen from Fig. 6 that main Cu $2P_{3/2}$ and Cu $2P_{1/2}$ peaks are accompanied by two low intensity peaks with higher binding energy at 941 and 960 eV. In addition, the core peak of the reduced sample, the Cu $2P_{3/2}$ peak can be fitted into two components at 934.5 and 932.5 eV which can be assigned as metallic Cu and mixture of Cu^{2+}/Cu^{+} ions according to the binding energy. It is worth mentioning that it is challenging to distinguish Cu^{2+} and Cu^{+} ions thanks to the close binding energies. Similar satellite peaks were also observed for Cu $2P_{1/2}$ at 955.4 and 953.1 eV. The presence of Ce^{4+}/Ce^{3+}, Cu^{2+}/Cu^{+} and oxygen vacancy confirmed by the XPS spectra suggests a strong interaction between well dispersed copper oxide species and CeO_2 NR enriched with surface defects through $Ce^{4+} + Cu^{+} \leftrightarrow Ce^{3+} + Cu^{2+}$ during redox treatments.

3.6. TEM analysis

Fig. 7 depicts the representative TEM images of the 10 wt% CuO/CeO_2 NR-o and 10 wt% CuO/CeO_2 NR-r catalysts to identify the particle morphology, size, and atomic level crystal/defect structures. It is clear that the CeO_2 NR support maintains the initial rod-like morphology after the deposition of 10 wt% of CuO for both oxidized and reduced samples.

From the images, the length and diameter of CeO_2 NR for the oxidized sample are in the range of 40 - 72 nm and 5 - 14 nm, respectively. However, CuO_x crystallites are hardly to be observed due to smaller size and possible strong CuO_x-CeO_2 interaction [18], which agrees with the XRD analysis (Fig. 1). Fig. 7(a & b) show the HRTEM images of local structures for the oxidized and reduced CeO_2 NR supported CuO_x samples, and lattice fringes analysis indicates that CuO_x clusters are embedded in CeO_2 NR.

Fig. 8 further analyzes the local defect structure and lattice d-spacings of the 10 wt% CuO/CeO_2 NR-o sample at different sites. In general, HRTEM images illustrate rough surfaces of CeO_2 NR with a combination of lattice distortion, void, and expanded or contracted lattice defects. It is known that defected surface of CeO_2 NR promotes strong metal-support interaction and the supported catalysts perform better low temperature performance of CO oxidation [42]. CeO_2 NR show dominant (111), (100) and (011) lattice fringes with corresponding d-spacing of 3.08-3.16 Å, 2.7Å and 1.9 Å respectively [24]. It is noted that, according to HRTEM lattice analysis, CeO_2 (111) was the richest termination surface for the prepared catalysts.

3.7. CO oxidation test

Fig. 9(a) presents the catalytic CO oxidation performances of the oxidized 10 wt% Cu/CeO_2 NR, 10 wt% Cu/CeO_2 NC and 10 wt% Cu/SiO_2 catalysts while Fig. 9(b) shows the CO oxidation performance of the reduced 10 wt% Cu/CeO_2 NR and 10 wt% Cu/CeO_2 NC samples. According to Fig. 9(c), pure CeO_2 support and CuO showed low catalytic activity for CO oxidation with T_{50} (50% CO conversion) at ~x223C320 °C and 220 °C, respectively. On the contrary, Fig. 9(a, b), it is clearly evidenced that the synergy effect of CuO_x and CeO_2 NR can improve the CO oxidation dramatically for both oxidized and reduced samples (T_{50}<100 °C). This synergism between CuO_x and CeO_2 NR has been reported previously [43,44]. Shown in Fig. 9(a), T_{50} for 10 wt% CuO/-CeO_2 NR-o was achieved at 88°C while for 10 wt% CuO/CeO_2 NC-o it was at 146°C. It can be clearly demonstrated that support morphology play significant effect on CO oxidation performance. However, both oxidized 10 wt% CuO/CeO_2 NR and 10 wt% CuO/CeO_2 NC samples showed approximately 90% CO conversion at 195°C, shows at Fig. 9(a). However, the reduction treatment decreased the conversion rate

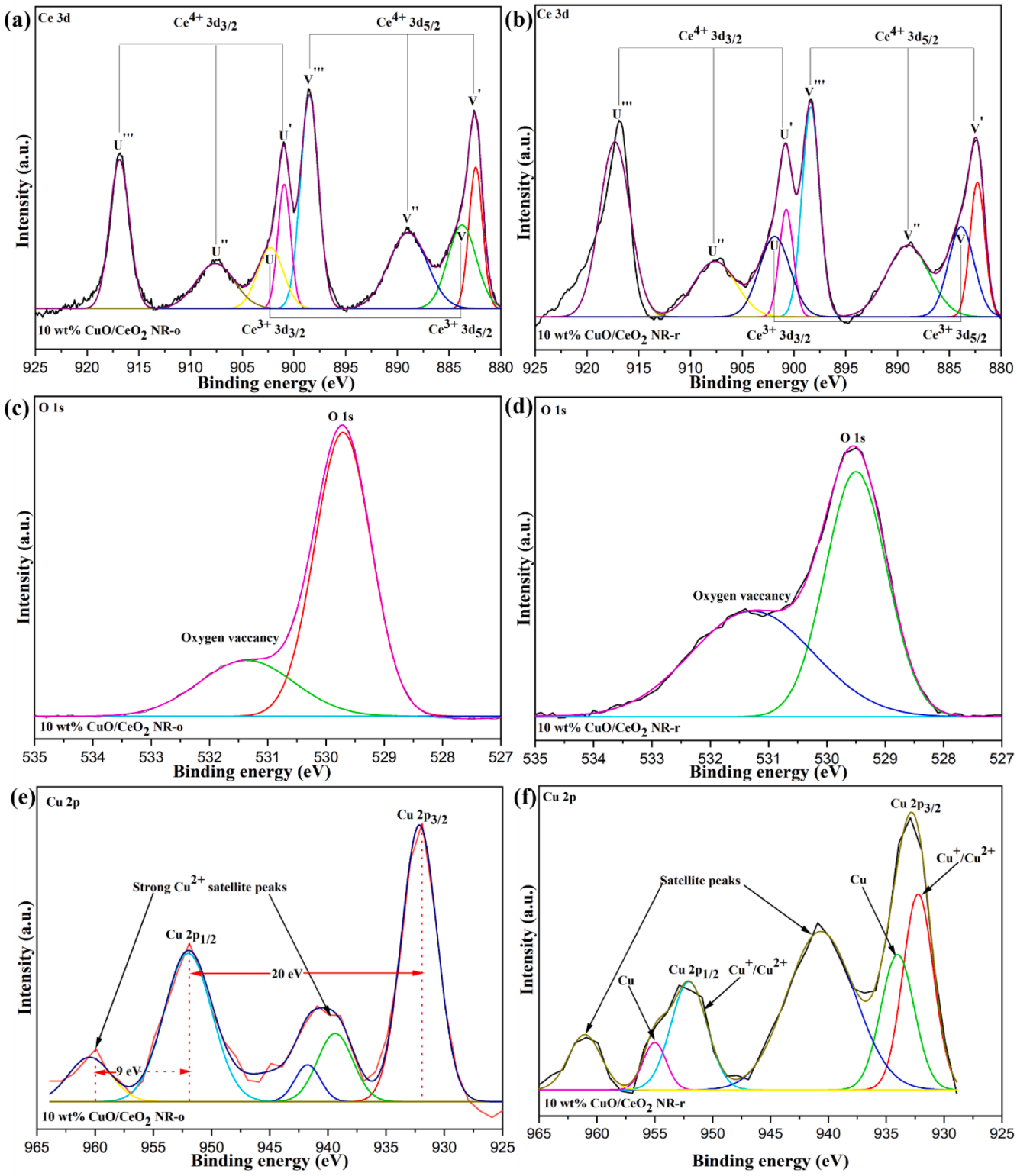

Fig. 6. XPS spectra of the 10 wt% CuO/CeO_2 NR samples after the oxidation and reduction treatments.

noticeably. For example, for oxidized and reduced 10 wt% CuO/CeO_2 NR from Fig. 9(a, b), at ~x223C55°C, the two samples have similar amount of CO conversion (<5%). At ~x223C100°C, the CO conversion jumps up to 62.8% for 10 wt% CuO/CeO_2 NR-o and 56.5% for 10 wt% CuO/CeO_2 NR-r. Above 300 °C, the conversion rate became stable and approached to 100% for 10 wt% CuO/CeO_2 NR-o. It is also clear that the 10 wt% CuO/CeO_2 NR-o sample shows better low temperature CO oxidation activity than that of the 10 wt% CuO/CeO_2 NR-r sample for all the temperature range. This is because the oxidized sample can provide more oxygen both from CuO crystallites and CeO_2 support for the oxidation of CO. After the reduction treatment most of the CuO species were reduced to Cu by three possible reduction routes: (1) $CuO \rightarrow Cu_4O_3 \rightarrow Cu_2O \rightarrow Cu$; (2) $CuO \rightarrow Cu_2O \rightarrow Cu$; and (3) $CuO \rightarrow Cu$. However, the reduced sample was able to perform CO conversion because of the

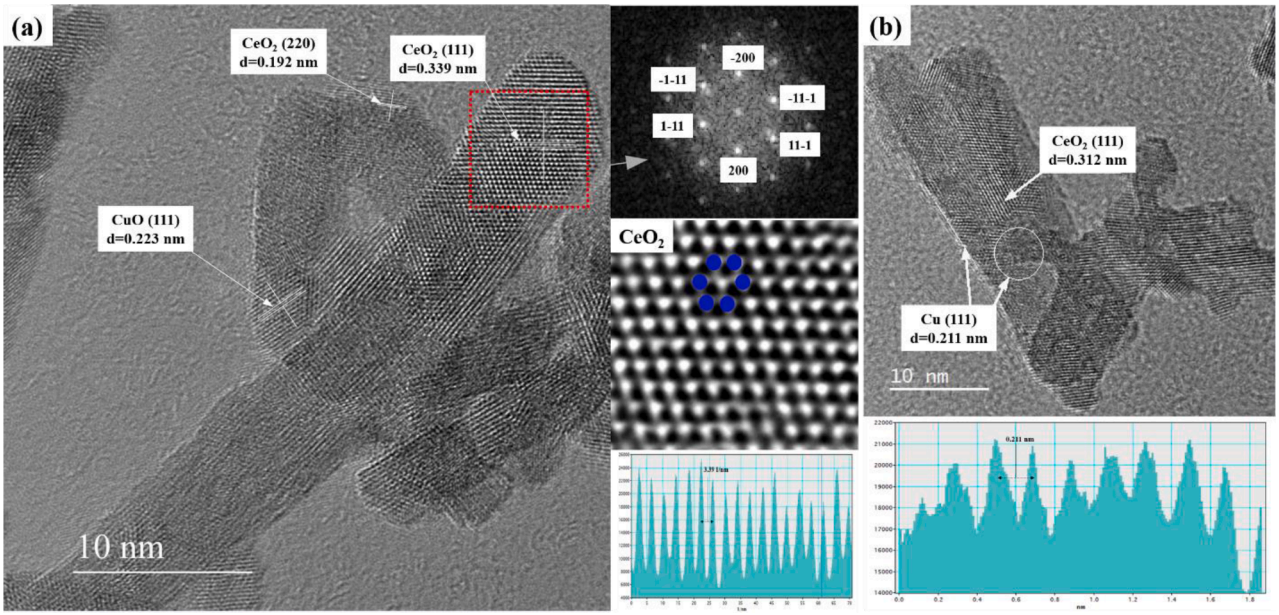

Fig. 7. TEM images and diffractogram/lattice fringe analysis of (a) 10 wt% CuO/CeO_2 NR-o and (b) 10 wt% CuO/CeO_2 NR-r.

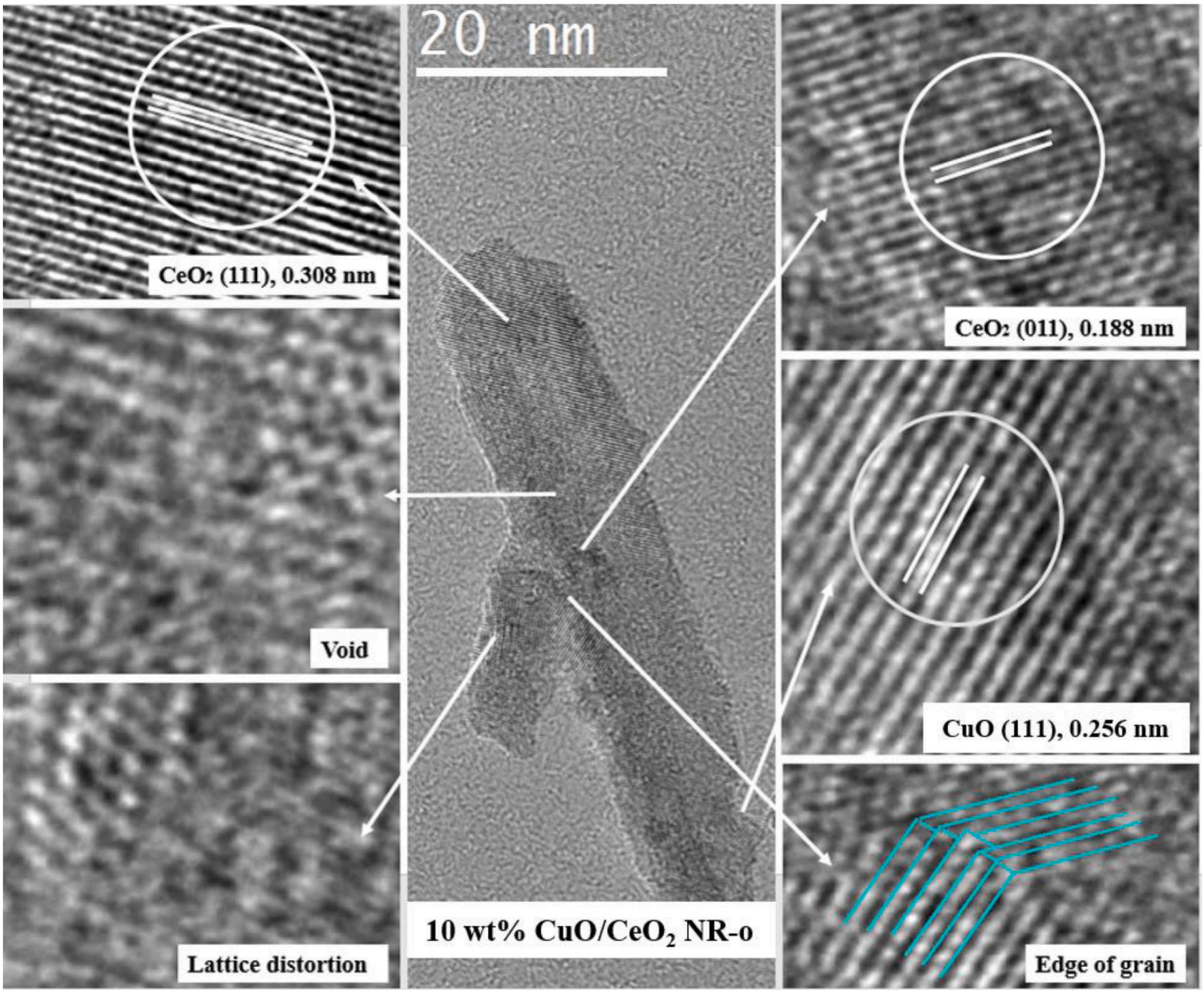

Fig. 8. HRTEM images of 10 wt% CuO/CeO_2 NR-o showing various defects.

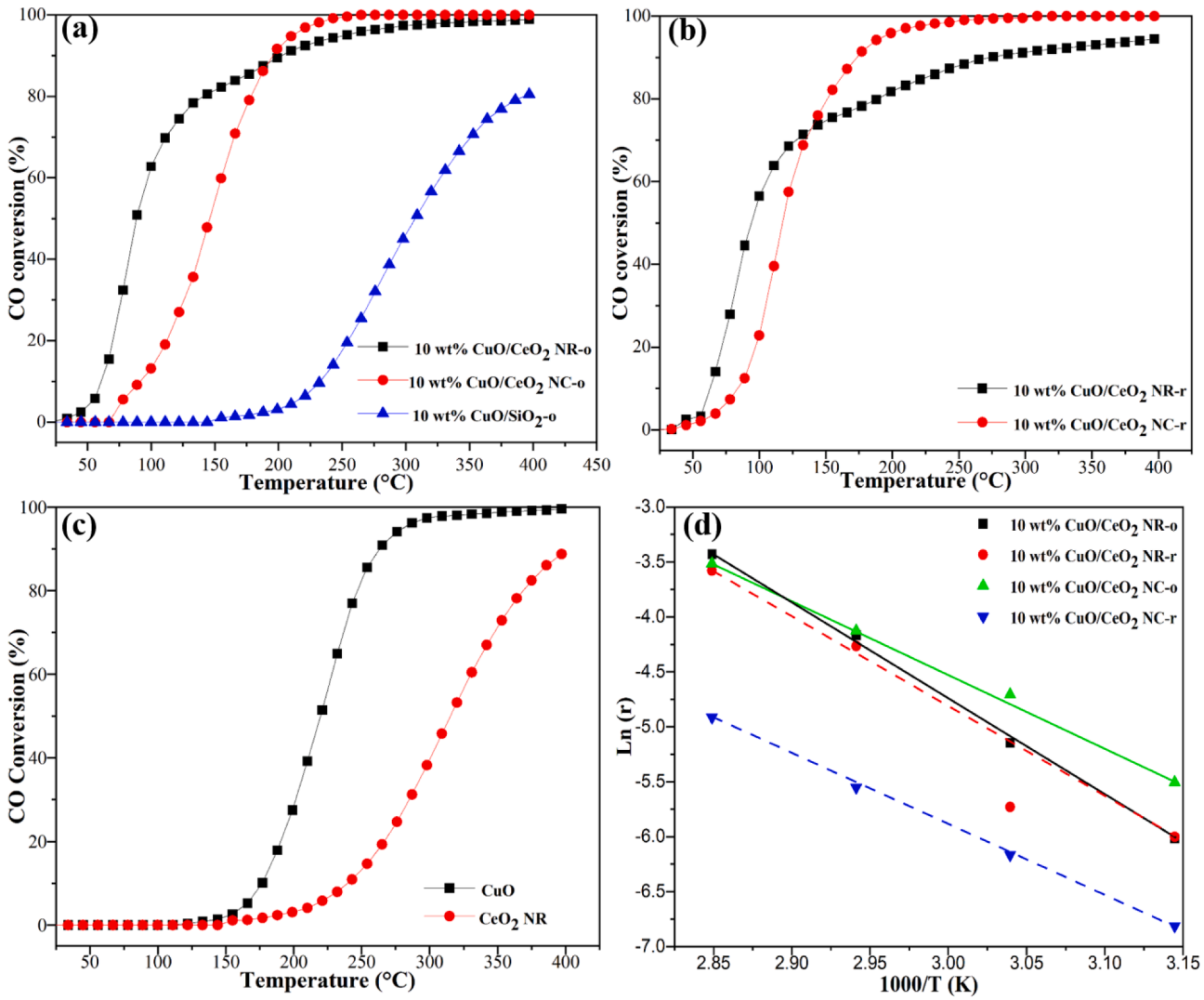

Fig. 9. CO oxidation conversion comparison of (a) 10 wt% CuO/CeO_2 NR-o, 10 wt% CuO/CeO_2 NC-o, and 10 wt% CuO/SiO_2–o; (b) 10 wt% CuO/CeO_2 NR-r and 10 wt% CuO/CeO_2 NC-r; (c) CuO and CeO_2 NR; (d) activation energy for 10 wt% CuO/CeO_2 NR-o, 10 wt% CuO/CeO_2 NR-r, 10 wt% CuO/CeO_2 NC-o, and 10 wt% CuO/CeO_2 NC-r.

reducibility property of CeO_2 NR by the equation: $2\ CeO_2 + CO = Ce_2O_3 + CO_2$ as well as the reduction of the Cu-O-Ce solid solution at the metal/support interface. In addition, some re-oxidized CuO_x species could also contribute to the CO oxidation which was evidenced by the H_2-TPR profile (Fig. 3). However, the 10 wt % CuO/SiO_2-o catalyst shows poor performance than those of CeO_2 supported catalysts thanks to the irreducibility of SiO_2. As shown in Fig. 9(d), the apparent activation energies (E_a) for the CeO_2 supported catalysts were calculated below 40% CO conversion using Arrhenius plot. The E_a values for 10 wt% CuO/CeO_2 NR-o, 10 wt% CuO/CeO_2 NR-r, 10 wt% CuO/CeO_2 NC-o and 10 wt% CuO/CeO_2 NC-r are 59.6 $kJmol^{-1}$, 59.6 $kJmol^{-1}$, 71.6 $kJmol^{-1}$ and 71.6 $kJmol^{-1}$, respectively. Table S1 presents a performance comparison between previously published results with similar catalysts and this work.

3.8. *In situ DRIFTS analysis*

To further explore CO adsorption and desorption behaviors on the prepared catalysts, *in situ* DRIFTS was carried out. Fig. 10(a-f) show the CO adsorption spectra over the 10 wt% CuO/CeO_2 NR-o and 10 wt% CuO/CeO_2 NR-r catalysts. It can be assumed that CO adsorption either occurred on CuO_x catalyst and/or CeO_2 support surfaces. Fig. 10(b-c and e-f) illustrate the zoomed regions from Fig. 10(a and d). From the literature, it was reported that CO adsorption on CeO_2 surface can form various carbonate, bicarbonate and formate species which can be observed from the peak ranges of 1000 cm^{-1}-1700 cm^{-1} [34, 35]. Fig. 10(b and e) show the most intense vibration modes of surface carbonates and other oxo-species for both oxidized and reduced samples. During CO adsorption, CO molecule acts as electron-donor probe and oxygen can capture these CO molecules and form carbonate, bicarbonate and formate species. In Fig. 10(b and e), there are ~x223C8 peaks combination with higher, medium and low intensity at wave number around 1062 cm^{-1}, 1216 cm^{-1}, 1297 cm^{-1}, 1351 cm^{-1}, 1392 cm^{-1}, 1544 cm^{-1}, 1574 cm^{-1}, and 1612 cm^{-1}. All of these peaks represent the formation of bi and tri carbonate as well as bridged carbonate, formate and carboxylates, the intensity of which gradually decreases with increasing temperature from 140°C [45]. This suggests that the surface carbonate and oxo-species formed through the conversion of CO started to desorb from the supported catalyst surface at higher temperature. The formed carbonate species on the surface of the supported catalysts may be a possible reason to limit the CO conversion rate and lower activity of catalyst because the active sites are blocked by these species, known as "surface poisoning" [44–46].

The adsorption of CO molecule over CuO crystallites is illustrated in Fig. 10(c and f) where a sharp peak was observed between the regions of 2050 cm^{-1}-2150 cm^{-1}. Several reports have shown previously that

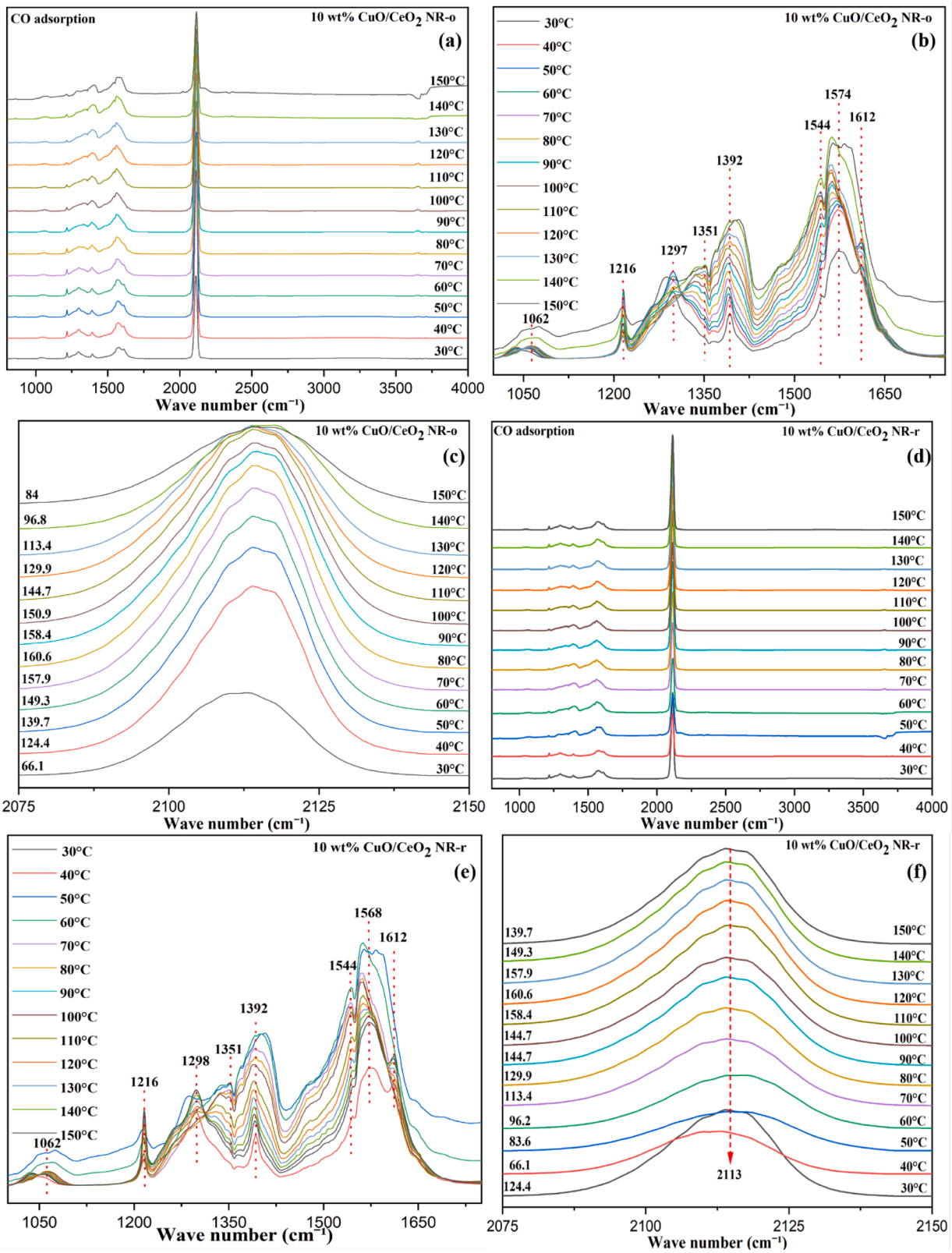

Fig. 10. DRIFTS spectra recorded after exposure to CO on (a) the oxidized 10 wt% CuO/ CeO_2 NR, (b-c) DRIFTS spectra of the oxidized 10 wt% CuO/CeO_2 NR catalyst for the regions of 1000 cm^{-1}-1750 cm^{-1} and 2075 cm^{-1}-2150 cm^{-1}, (d) DRIFTS spectra of the reduced 10 wt% CuO/CeO_2 NR, (e-f) DRIFTS spectra of the reduced 10 wt% CuO/CeO_2 NR catalyst for the regions of 1000 cm^{-1}-1750 cm^{-1} and 2075 cm^{-1}-2150 cm^{-1}.

there are three CO adsorption band available for CuO_x sites. These ranges are 2200-2140, 2140-2100, and 2100-2000 cm^{-1} which represent the CO adsorption on Cu (ii), Cu (i) and Cu (0) sites, respectively [47–49].

However, in our DRIFTS results, one single broad band peak at 2113 cm^{-1} was observed, which might be an overlap of two or three peaks from CO adsorption on Cu (ii), Cu (i) and Cu (0) sites. The H_2-TPR and CO-TPD results suggest the presence of Cu^+ and Cu^{2+} species. Deng et al. [50] and Dong et al. [51] reported that at ambient temperature, Cu^+-CO adsorption was more stable than others. For Fig. 10(c), it was found that this adsorption peak intensity first increased with temperature till 80°C and then started to decrease with the increasing temperature till 150°C. The integrated peak area of the curve for each temperature is listed on the left sides in Fig. 10(c, f) to quantitatively illustrate the change of the amount of the adsorbed molecules with temperature. These results can be explained as follows: initially, CO adsorption occurs at CuO_x sites till 80°C. From 80°C to 150°C, the peak area of the band decreases, which can be attributed to the interaction of CO with Cu^+ and Cu^{2+} ions leading to the reduction from CuO→Cu_2O→Cu and less active adsorption sites.

4. Conclusion

Among SiO_2, CeO_2 NR and CeO_2 NC supported CuO_x, the CeO_2 NR supported CuO_x catalyst shows the best low temperature catalytic performance of CO oxidation, mainly due to the higher surface defects of CeO_2 NR support including high concentration of Ce^{3+}, oxygen vacancy, other surface defects which significantly promote a strong interaction with CuO_x clusters and surface oxygen release capability at lower temperature. The interaction of the supported CuO_x catalyst with CO by CO-TPD data confirmed that 10 wt% CuO/CeO_2 NR-o showed the highest CO/CO_2 desorption capability at the lowest temperature of 89°C, which was further studied by *in situ* DRIFTS experiments. In addition, it is concluded from the *in situ* DRIFTS results that the highest CO adsorption on the CeO_2 NR supported CuO_x catalysts occurred around 80°C~x223C90°C and at the higher temperature the adsorbed CO amount started to decrease partially due to the reduction of CuO through CuO→Cu_2O→Cu and the decreased active adsorption sites. These results point out a promising strategy to enhance the catalyst activity via charge and mass transfer and tuned interaction between catalyst clusters and oxide supports.

CRediT authorship contribution statement

Md Robayet Ahasan: Investigation, Methodology, Formal analysis, Writing – original draft, Writing – review & editing. **Yifan Wang:** Formal analysis, Writing – review & editing. **Ruigang Wang:** Conceptualization, Investigation, Methodology, Supervision, Formal analysis, Writing – review & editing, Funding acquisition.

Declaration of Competing Interest

The authors declare that they have no known competing financial interests or personal relationships that could have appeared to influence the work reported in this paper.

Acknowledgement

This project is supported by the grants from the National Science Foundation (CBET 1856729 and IIP 2044733). The use of electron microscopy facilities at the Alabama Analytical Research Center (AARC) at The University of Alabama is gratefully acknowledged.

References

[1] A.I. Boronin, et al., CO oxidation activity of Pt/CeO2 catalysts below 0°C: platinum loading effects, Appl. Catal. B Environ. 286 (2021), 119931, https://doi.org/10.1016/j.apcatb.2021.119931.
[2] S. Rood, S. Eslava, A. Manigrasso, C. Bannister, Recent advances in gasoline three-way catalyst formulation: a review, Proc. Inst. Mech. Eng. Part D J. Automob. Eng. 234 (4) (2020) 936–949.
[3] N.S. Portillo-Vélez, R. Zanella, Comparative study of transition metal (Mn, Fe or Co) catalysts supported on titania: effect of Au nanoparticles addition towards CO oxidation and soot combustion reactions, Chem. Eng. J. 385 (2020), 123848.
[4] X. Xie, Y. Li, Z.-Q. Liu, M. Haruta, W. Shen, Low-temperature oxidation of CO catalysed by Co3O4 nanorods, Nature 458 (7239) (2009) 746–749, https://doi.org/10.1038/nature07877.
[5] Y. Lou, et al., Identification of active area as active center for CO oxidation over single Au atom catalyst, ACS Catal. 10 (11) (Jun. 2020) 6094–6101, https://doi.org/10.1021/acscatal.0c01303.
[6] Y. Lou, et al., Promoting effects of In2O3 on Co3O4 for CO oxidation: tuning O2 activation and CO adsorption strength simultaneously, ACS Catal. 4 (11) (Nov. 2014) 4143–4152, https://doi.org/10.1021/cs501049r.
[7] W. Liu, M. Flytzani-Stephanopoulos, Transition metal-promoted oxidation catalysis by fluorite oxides: a study of CO oxidation over CuO CeO2, Chem. Eng. J. Biochem. Eng. J. 64 (2) (1996) 283–294.
[8] G. Spezzati, et al., CO oxidation by Pd supported on CeO2 (100) and CeO2 (111) facets, Appl. Catal. B Environ. 243 (2019) 36–46.
[9] N.J. Lawrence, et al., Defect engineering in cubic cerium oxide nanostructures for catalytic oxidation, Nano Lett 11 (7) (2011) 2666–2671.
[10] J.A. Rodríguez, J. Hrbek, Inverse oxide/metal catalysts: a versatile approach for activity tests and mechanistic studies, Surf. Sci. 604 (3–4) (2010) 241–244.
[11] T. Montini, M. Melchionna, M. Monai, P. Fornasiero, Fundamentals and catalytic applications of CeO2-based materials, Chem. Rev. 116 (10) (2016) 5987–6041.
[12] J. Zhao, et al., Suppressing metal leaching in a supported Co/SiO2 catalyst with effective protectants in the hydroformylation reaction, ACS Catal. 10 (2) (2019) 914–920.
[13] J. Vicente, C. Montero, J. Ereña, M.J. Azkoiti, J. Bilbao, A.G. Gayubo, Coke deactivation of Ni and Co catalysts in ethanol steam reforming at mild temperatures in a fluidized bed reactor, Int. J. Hydrogen Energy 39 (24) (2014) 12586–12596, https://doi.org/10.1016/j.ijhydene.2014.06.093.
[14] P. Liu, J.A. Rodriguez, Water-gas-shift reaction on metal nanoparticles and surfaces, J. Chem. Phys. 126 (16) (2007), 164705.
[15] K. Song, et al., Effect of alloy composition on catalytic performance and coke-resistance property of Ni-Cu/Mg (Al) O catalysts for dry reforming of methane, Appl. Catal. B Environ. 239 (2018) 324–333.
[16] C. Paolucci, J.R. Di Iorio, F.H. Ribeiro, R. Gounder, W.F. Schneider, Catalysis science of NOx selective catalytic reduction with ammonia over Cu-SSZ-13 and Cu-SAPO-34, in: Advances in Catalysis, 59, Elsevier, 2016, pp. 1–107.
[17] G. Wu, N. Guan, L. Li, Low temperature CO oxidation on Cu–Cu 2 O/TiO 2 catalyst prepared by photodeposition, Catal. Sci. Technol. 1 (4) (2011) 601–608.
[18] A.-P. Jia, S.-Y. Jiang, J.-Q. Lu, M.-F. Luo, Study of catalytic activity at the CuO−CeO2 interface for CO oxidation, J. Phys. Chem. C 114 (49) (Dec. 2010) 21605–21610, https://doi.org/10.1021/jp108556u.
[19] M.-F. Luo, Y.-P. Song, J.-Q. Lu, X.-Y. Wang, Z.-Y. Pu, Identification of CuO species in high surface area CuO−CeO2 catalysts and their catalytic activities for CO oxidation, J. Phys. Chem. C 111 (34) (Aug. 2007) 12686–12692, https://doi.org/10.1021/jp0733217.
[20] S.T. Hossain, E.T. Zell, S. Balaz, R. Wang, A γ to α type transition of CuO species over CeO2-SiO2 composites supported CuO catalysts, Appl. Surf. Sci. 491 (2019) 374–382.
[21] R. Wang, R. Dangerfield, Seed-mediated synthesis of shape-controlled CeO 2 nanocrystals, RSC Adv. 4 (7) (2014) 3615–3620.
[22] A.K. Prodjosantoso, I.S. Farrasiya, K.S. Budiasih, M.P. Utomo, The use of silica supported nickel-copper oxide catalyst for photodegradation of methylene blue, Orient. J. Chem. 35 (4) (2019) 1414.
[23] T. Naganuma, Shape design of cerium oxide nanoparticles for enhancement of enzyme mimetic activity in therapeutic applications, Nano Res. 10 (1) (2017) 199–217.
[24] S.A. Mock, E.T. Zell, S.T. Hossain, R. Wang, Effect of reduction treatment on CO oxidation with CeO2 nanorod-supported CuOx catalysts, ChemCatChem 10 (1) (2018) 311–319.
[25] S. Lomate, A. Sultana, T. Fujitani, Effect of SiO 2 support properties on the performance of Cu–SiO 2 catalysts for the hydrogenation of levulinic acid to gamma valerolactone using formic acid as a hydrogen source, Catal. Sci. Technol. 7 (14) (2017) 3073–3083.
[26] J.-Q. Lu, C.-X. Sun, N. Li, A.-P. Jia, M.-F. Luo, Kinetic study of CO oxidation over CuO/MO2 (M=Si, Ti and Ce) catalysts, Appl. Surf. Sci. 287 (2013) 124–134, https://doi.org/10.1016/j.apsusc.2013.09.091.
[27] D.Z. Gao, J. Strand, M.S. Munde, A.L. Shluger, Mechanisms of oxygen vacancy aggregation in SiO2 and HfO2, Front. Phys. 7 (2019) 43.
[28] K. Zhou, X. Wang, X. Sun, Q. Peng, Y. Li, Enhanced catalytic activity of ceria nanorods from well-defined reactive crystal planes, J. Catal. 229 (1) (2005) 206–212.
[29] H.P. Sun, et al., Partial encapsulation of Pd particles by reduced ceria-zirconia, Appl. Phys. Lett. 87 (20) (2005), 201915.
[30] Y. Liu, D. Mao, J. Yu, Y. Zheng, X. Guo, Facile preparation of highly active and stable CuO–CeO 2 catalysts for low-temperature CO oxidation via a direct solvothermal method, Catal. Sci. Technol. 10 (24) (2020) 8383–8395.

[31] W. Shen, D. Mao, Z. Luo, J. Yu, CO oxidation on mesoporous SBA-15 supported CuO–CeO 2 catalyst prepared by a surfactant-assisted impregnation method, RSC Adv. 7 (44) (2017) 27689–27698.
[32] Z. Luo, D. Mao, W. Shen, Y. Zheng, J. Yu, Preparation and characterization of mesostructured cellular foam silica supported Cu–Ce mixed oxide catalysts for CO oxidation, RSC Adv. 7 (16) (2017) 9732–9743.
[33] S.U.N. Shuaishuai, M.A.O. Dongsen, Y.U. Jun, Enhanced CO oxidation activity of CuO/CeO2 catalyst prepared by surfactant-assisted impregnation method, J. Rare Earths 33 (12) (2015) 1268–1274.
[34] M. Guo, J. Lu, Y. Wu, Y. Wang, M. Luo, UV and visible Raman studies of oxygen vacancies in rare-earth-doped ceria, Langmuir 27 (7) (2011) 3872–3877.
[35] M. Koenig, et al., Salt sensitivity of the thermoresponsive behavior of PNIPAAm brushes, Langmuir 34 (7) (2018) 2448–2454.
[36] A. Filtschew, K. Hofmann, C. Hess, Ceria and its defect structure: new insights from a combined spectroscopic approach, J. Phys. Chem. C 120 (12) (2016) 6694–6703.
[37] A.-P. Jia, G.-S. Hu, L. Meng, Y.-L. Xie, J.-Q. Lu, M.-F. Luo, CO oxidation over CuO/Ce1− xCuxO2− δ and Ce1− xCuxO2− δ catalysts: synergetic effects and kinetic study, J. Catal. 289 (2012) 199–209.
[38] Y. Jiangrong, W. Xiaolin, J. Chunli, X. Hong, L. Lei, An AES study of the initial stages of oxidation of cerium, Surf. Interface Anal. An Int. J. Devoted Dev. Appl. Tech. Anal. Surf., Interfaces thin Film 38 (4) (2006) 498–501.
[39] F. Larachi, J. Pierre, A. Adnot, A. Bernis, Ce 3d XPS study of composite CexMn1− xO2− y wet oxidation catalysts, Appl. Surf. Sci. 195 (1–4) (2002) 236–250.
[40] E. Bêche, P. Charvin, D. Perarnau, S. Abanades, G. Flamant, Ce 3d XPS investigation of cerium oxides and mixed cerium oxide (CexTiyOz, Surf. Interface Anal. An Int. J. Devoted Dev. Appl. Tech. Anal. Surf., Interfaces thin Film 40 (3–4) (2008) 264–267.
[41] Z. Liu, J. Li, M. Buettner, R.V Ranganathan, M. Uddi, R. Wang, Metal–support interactions in CeO2- and SiO2-supported cobalt catalysts: effect of support morphology, reducibility, and interfacial configuration, ACS Appl. Mater. Interfaces 11 (18) (May 2019) 17035–17049, https://doi.org/10.1021/acsami.9b02455.
[42] S.A. Mock, S.E. Sharp, T.R. Stoner, M.J. Radetic, E.T. Zell, R. Wang, CeO2 nanorods-supported transition metal catalysts for CO oxidation, J. Colloid Interface Sci. 466 (2016) 261–267.
[43] S. Chen, et al., Anchoring high-concentration oxygen vacancies at interfaces of CeO2–x/Cu toward enhanced activity for preferential CO oxidation, ACS Appl. Mater. Interfaces 7 (41) (Oct. 2015) 22999–23007, https://doi.org/10.1021/acsami.5b06302.
[44] J. Li, Y. Han, Y. Zhu, R. Zhou, Purification of hydrogen from carbon monoxide for fuel cell application over modified mesoporous CuO–CeO2 catalysts, Appl. Catal. B Environ. 108 (2011) 72–80.
[45] H. Zhu, Y. Chen, Z. Wang, W. Liu, L. Wang, Catalytic oxidation of CO over mesoporous copper-doped ceria catalysts via a facile CTAB-assisted synthesis, RSC Adv. 8 (27) (2018) 14888–14897.
[46] L. Qi, et al., Influence of cerium precursors on the structure and reducibility of mesoporous CuO-CeO2 catalysts for CO oxidation, Appl. Catal. B Environ. 119–120 (2012) 308–320, https://doi.org/10.1016/j.apcatb.2012.02.029.
[47] C. Wang, et al., Probing effective photocorrosion inhibition and highly improved photocatalytic hydrogen production on monodisperse PANI@ CdS core-shell nanospheres, Appl. Catal. B Environ. 188 (2016) 351–359.
[48] L. Lin, et al., In situ characterization of Cu/CeO2 nanocatalysts for CO2 hydrogenation: morphological effects of nanostructured ceria on the catalytic activity, J. Phys. Chem. C 122 (24) (Jun. 2018) 12934–12943, https://doi.org/10.1021/acs.jpcc.8b03596.
[49] Y.A. May, W.-W. Wang, H. Yan, S. Wei, C.-J. Jia, Insights into facet-dependent reactivity of CuO–CeO2 nanocubes and nanorods as catalysts for CO oxidation reaction, Chin. J. Catal. 41 (6) (2020) 1017–1027, https://doi.org/10.1016/S1872-2067(20)63533-1.
[50] C. Deng, et al., NO reduction by CO over CuO supported on CeO2-doped TiO2: the effect of the amount of a few CeO2, Phys. Chem. Chem. Phys. 17 (24) (2015) 16092–16109, https://doi.org/10.1039/C5CP00745C.
[51] L. Dong, et al., Influence of molar ratio and calcination temperature on the properties of TixSn1−xO2 supporting copper oxide for CO oxidation, Appl. Catal. B Environ. 180 (2016) 451–462, https://doi.org/10.1016/j.apcatb.2015.06.034.